

Study on impurity hole plasmas by global neoclassical simulation

Keiji Fujita¹ S. Satake^{1,2} M. Nunami^{1,2} J. M. García-Regaña³
J. L. Velasco³ I. Calvo³

¹ The Graduate University for Advanced Studies (SOKENDAI), 322-6 Oroshi-cho, Toki, Japan

² National Institute for Fusion Science 322-6 Oroshi-cho, Toki, Japan

³ Laboratorio Nacional de Fusión, CIEMAT, Avenida Complutense, 40, 28040, Madrid, Spain

E-mail: fujita.keiji@nifs.ac.jp

May 2021

Abstract. An impurity hole observed in the Large Helical Device (LHD) is a hollow density profile of an impurity ion species formed in the core plasma where the negative (inward-pointing) ambipolar radial electric field (E_r) exists. Although local neoclassical models have predicted that the sign of E_r in impurity hole plasmas is negative for the entire minor radius, an experimental measurement of an impurity hole plasma has shown that the E_r changes the sign from negative to positive along the minor radius. In the present work, we investigate neoclassical impurity transport in an impurity hole plasma using a global neoclassical simulation code FORTEC-3D. The variation of electrostatic potential on each flux surface (Φ_1) is evaluated from the quasi-neutrality condition in multi-ion-species plasma by the global simulation. The ambipolar E_r and neoclassical fluxes are determined in solving a global drift-kinetic equation including the effect of Φ_1 . By the global simulation, we show that an E_r which changes the sign along the radius is obtained as a solution of the ambipolar condition and with such an E_r , impurity carbon flux can be outwardly directed even where $E_r < 0$ and the carbon density profile is hollow around the magnetic axis. Furthermore, it is found that the outward carbon flux is only a factor 2-3 from balancing the modeled inward turbulent flux. Our result indicates that we have moved one step closer to reproducing the impurity transport in impurity hole plasmas by kinetic simulation.

1. Introduction

In addition to fuel deuterium or tritium, fusion plasmas contain a variety of ions including helium produced by fusion reactions or high- Z ions such as tungsten or iron sputtered from the wall. The presence of such impurity ions in the core plasma can degrade the performance of the fusion reactor by diluting the fuel ions and radiating a significant amount of energy away. Ions with higher charges cause those unfavourable effects more significantly. Understanding the impurity transport process to prevent the

impurity accumulation is thus a crucial task to realize the steady-state operation of fusion reactors.

In stellarator and heliotron type devices, the ambipolar radial electric field, E_r , can play a crucial role in determining the behavior of impurity ions. In fusion relevant plasma, in which the electron temperature T_e and the ion temperature T_i are comparable, the sign of the ambipolar E_r usually becomes negative [1, 2]. Ion species are thus driven inwardly by the negative E_r and its impact is proportional to the charge Z . In this aspect, tokamaks have an advantage over stellarators. In tokamaks, neoclassical transport is intrinsically ambipolar and is independent of the ambipolar radial electric field. A sufficiently large temperature gradient can thus drive the impurity ions out of the core. This is called “temperature screening” [3]. Although it is shown that the contribution of the terms involving the E_r to the radial impurity flux can be cancelled even in stellarators, the condition for the effect to take place is rather strict [4, 5, 6, 7, 8, 9].

The prediction of impurity accumulation under the condition discussed above has been confirmed by experiments [10], but a few exceptional cases have been observed as well. One of the exceptions is observation of the so-called “impurity holes” in the LHD [11, 12], which indicates the formation of hollow impurity density profiles in the core. Neoclassical transport simulations have predicted negative ambipolar E_r and inward-pinch of carbon impurity for the impurity hole plasmas [11, 13, 14, 15]. Gyrokinetic studies have also predicted inward impurity turbulent flux in impurity hole plasmas [16, 17, 18]. Therefore, there should be other mechanisms to explain the exhaust of impurity ions from the center of the plasmas.

The increase in the ion temperature and its gradient, which characterizes an impurity hole plasma, is thought to play an essential role in the impurity hole formation. If the size of the negative E_r is small and the temperature gradient is sufficiently large, it is shown that the exhaust of impurity ions by the temperature gradient is in fact possible even when the negative E_r does contribute to the radial transport [15, 19]. However, according to the analysis, the ion temperature should be even higher than observed to overcome the inward pinch of moderate- Z (namely, $Z = 6$ for carbon) and high- Z impurities caused by the negative E_r and the positive impurity density gradient.

In order to provide an explanation for the mechanism behind the impurity hole formation, a variety of attempts to extend the neoclassical analysis have been made. In [20], the possibility that the ambipolar E_r is shifted to be positive by an external torque and the radial carbon flux becomes outward is shown. To change the sign of the E_r , however, a fairly stronger external torque than a tangential neutral beam injection (NBI) torque input in LHD experiments is expected to be required.

Another approach to extension is to consider the effect of the variation of electrostatic potential on each flux surface, which has recently been shown to have non-negligible impact on impurity transport [6, 14, 15, 21, 22]. The variation of electrostatic potential is defined as the non-flux function part of the electrostatic potential, $\Phi_1 \equiv \Phi - \Phi_0$, where Φ is the total electrostatic potential and $\Phi_0 = \Phi_0(r)$

is the flux function part of Φ . Still, the neoclassical simulations for the impurity hole plasmas have shown that the E_r is negative along the entire radius and the carbon flux is driven further inwardly by the effect of Φ_1 [14, 15].

The E_r profile has been measured with a heavy ion beam probe (HIBP) in an LHD plasma in which an impurity hole formation is observed [13]. The measurement shows that the E_r is indeed negative from the magnetic axis to $r/a = 0.55$ as predicted by the neoclassical simulations, where r is the radial coordinate and a is the minor radius. However, the same experimental data shows that the sign of the E_r transits from negative to positive around $r/a = 0.55$ [13, 23]. The neoclassical predictions are thus, in fact, not accurate for $r/a > 0.55$. Still, it is mentioned in [19] that the condition of high- T plasmas is close to that for E_r to be positive. This suggests a possibility that the observed profile can be numerically reproduced by improving the neoclassical simulation model.

The preceding numerical studies on the impurity neoclassical transport in the impurity hole plasmas have been carried out with the radially-local drift-kinetic models, in which the magnetic drift velocity (grad- B and curvature drift) of guiding-center motion is treated as a negligibly small quantity compared with the parallel and the $E \times B$ velocities. On the other hand, a global neoclassical transport code FORTEC-3D [24, 25, 26] has been developed to solve a drift-kinetic equation without relying on the radially-local approximation and taking the finite magnetic drift across the magnetic field line and the flux surface into account. Using FORTEC-3D, it has been revealed that the local approximation is inaccurate to evaluate the neoclassical transport in helical plasmas when $|E_r|$ is small and the $E \times B$ -drift velocity is comparable to the magnetic drift velocity [27, 28], especially for ions and in non-neoclassical-optimized magnetic configuration such as in LHD.

After extending the code for multi-particle species plasmas [29], the first applications of FORTEC-3D code to LHD impurity hole plasmas have been carried out in the trace-impurity limit, in which the ambipolar E_r and Φ_1 are assumed to be determined only from bulk hydrogen and electrons. Through those applications, it has been found that the Φ_1 potential profile on each flux surface obtained by the global calculation is different from that obtained with the local approximation models [30] and that the E_r profile in the LHD impurity hole plasma is expected to be positive for almost the entire region [31]. It has also been found that the positive E_r results in outward carbon impurity flux and the Φ_1 -effect further enhances the outward flux. The global neoclassical simulation model thus becomes a candidate to explain the impurity hole phenomena found in LHD. However, there remain several issues to be considered. First, the HIBP measurement detects the negative E_r region in the center of an impurity hole plasma, which is inconsistent with the expectation from the FORTEC-3D simulation result. Second, the ambipolar E_r and Φ_1 have not been solved self-consistently in the trace-impurity limit. In order to increase the reliability of calculations, we have thus enabled our code to simultaneously solve the quasi-neutrality condition to evaluate Φ_1 , the ambipolar condition to determine the ambipolar E_r , and a drift-kinetic equation for

multiple ion species including Φ_1 .

In this article, we investigate the impurity hole plasma with the improved global code. In the next section, we present the numerical model used in our calculation and show how we evaluate the radial particle flux, ambipolar radial electric field, and Φ_1 . In section 3 the conditions of the plasma, such as the magnetic field configuration and the n - T profiles, are shown. In section 4, the simulation results are shown and compared with previous studies. The most striking outcomes of the global simulations are the ambipolar E_r profile which is negative near the magnetic axis but transits to positive along the minor radius and the outward carbon flux in the negative E_r region. Since the characteristic E_r profile is obtained regardless of the effect of Φ_1 and without the impact of NBI heating, it is indicated that the high-temperature profiles play a crucial role behind the E_r root-transitioning as discussed in [19]. The results are summarized and discussed in section 5.

2. Theoretical model

2.1. Drift-kinetic equation

In the global neoclassical model, plasma particles follow the equations of the guiding-center motion in five-dimensional phase space. As the phase variables, here we choose the guiding-center position \mathbf{X} , the parallel velocity v_{\parallel} and the magnetic moment $\mu = m_a v_{\perp}^2 / (2B)$, where m_a denotes the mass of the species a , v_{\perp} the perpendicular velocity, and B the strength of the magnetic field \mathbf{B} . In these coordinates, the equations of motion in static magnetic field are

$$\dot{\mathbf{X}} = v_{\parallel} \mathbf{b} + \frac{1}{Z_a e B_{\parallel}^*} \mathbf{b} \times (m_a v_{\parallel}^2 \mathbf{b} \cdot \nabla \mathbf{b} + \mu \nabla B + Z_a e \nabla \Phi), \quad (1)$$

$$\dot{v}_{\parallel} = - \frac{1}{m_a v_{\parallel}} \dot{\mathbf{X}} \cdot (\mu \nabla B + Z_a e \nabla \Phi), \quad (2)$$

$$\dot{\mu} = 0, \quad (3)$$

where $\mathbf{b} = \mathbf{B}/B$ is the unit vector along the magnetic field line, Z_a is the charge of the species a , $\mathbf{B}^* = \nabla \times \mathbf{A}^*$ is the corrected magnetic field with the guiding-center vector potential $\mathbf{A}^* = \mathbf{A} + m_a v_{\parallel} \mathbf{b} / (Z_a e)$, and $B_{\parallel}^* = \mathbf{B}^* \cdot \mathbf{b}$ and the overdot denotes the total time derivative. Note here that we do not use any approximation based on the order estimation $\Phi_0 \gg \Phi_1$, and therefore Φ_1 is included in all the terms involving Φ in the equations (1) and (2). According to the form of the equations (1) and (2), one can see that the relative importance of $\nabla \Phi_1$ term to the magnetic drift and magnetic mirror terms increases for higher Z_a .

FORTEC-3D solves the equation for $f_{a1} \equiv f_a - f_{a0}$, where f_a is the total distribution function of the species a and the analytically known part f_{a0} is given by

$$f_{a0} = f_{aM} e^{-Z_a e \Phi_1 / T_a}, \quad (4)$$

with the local Maxwellian

$$f_{aM} = n_{a0} \left(\frac{m_a}{2\pi T_a} \right)^{3/2} \exp \left(-\frac{m_a v_{\parallel}^2}{2T_a} - \frac{\mu B}{T_a} \right), \quad (5)$$

where the density n_{a0} and the temperature T_a are flux functions. As described in [31], f_{a0} does not contribute to the radial fluxes when both the magnetic drift and the $E \times B$ -drift due to Φ_1 are considered.

The first order drift-kinetic equation for f_{a1} is then given by

$$\begin{aligned} \frac{\partial f_{a1}}{\partial t} + \dot{\mathbf{X}} \cdot \nabla f_{a1} + \dot{v}_{\parallel} \frac{\partial f_{a1}}{\partial v_{\parallel}} - C_{TP}(f_{a1}) &= C_{FP}(f_{a0}) + \frac{Z_a e}{T_a} \frac{\partial \Phi_1}{\partial t} \\ - \dot{\mathbf{X}} \cdot \nabla_r \left[\frac{n'_{a0}}{n_{a0}} + \frac{Z_a e \Phi'_0}{T_a} + \left(\frac{m_a v_{\parallel}^2}{2T_a} + \frac{\mu B}{T_a} - \frac{3}{2} + \frac{Z_a e \Phi_1}{T_a} \right) \frac{T'_a}{T_a} \right] & f_{a0} \end{aligned} \quad (6)$$

where the prime denotes the derivative with respect to the radial coordinate r and $C_{TP}(f_{a1})$ and $C_{FP}(f_{a0})$ are the test particle part and the field particle part of the linearized collision operator, respectively,

$$C_{TP}(f_{a1}) = \sum_b C_{TP}^{ab}(f_{a1}, f_{b0}) \simeq \sum_b C_{TP}^{ab}(f_{a1}, f_{bM}) \quad (7)$$

$$C_{FP}(f_{a0}) = \sum_b C_{FP}^{ab}(f_{a0}, f_{b1}) \simeq \sum_b C_{FP}^{ab}(f_{aM}, f_{b1}). \quad (8)$$

In this work, the conventional Sugama model is used for the collision operator [29, 32]. The recent developments of the collision operator to include higher order terms, which have been neglected but can be important for impurity transport [9, 33], are not considered.

The equations (1)-(6) are reduced to those for a case without Φ_1 by setting $\Phi_1 = 0$. FORTEC-3D employs the two weight δf scheme to solve (6). See [31] and references therein for a derivation of (6) and the details of the numerical scheme.

3. Set up for the calculation

3.1. Particle species and electromagnetic fields

In this study, we investigate an LHD plasma with the standard configuration with a major radius of $R_0 = 3.7$ m and a minor radius of $a = 0.62$ m. The magnetic field strength and its major Fourier components in the Boozer coordinates are represented in Figure 1. The plasma contains two different impurity species, helium He^{2+} and carbon C^{6+} , as well as the main ion species, hydrogen H^{1+} . Since solving electrons together requires roughly 50 times the numerical cost, the drift-kinetic equation is solved only for the ions by the global code. Collisions of the ions with the electrons are also neglected.

When solving the ambipolar condition, electron flux evaluated with a local neoclassical code PENTA [34] is used. The Φ_1 -effect is not considered in the electron flux. Also, the contribution of the non-adiabatic variation of the electron density $n_{e1} \equiv \int d^3v f_{e1}$ is neglected in determining Φ_1 . The first approximation is justified

since the impact of Φ_1 on the electron flux is as small as that on the hydrogen flux, which is, as will be shown below, negligible especially in the near-axis region. The second approximation is by $f_{e1}/f_{i1} \sim \rho_e/\rho_i \ll 1$ when $T_i \sim T_e$, where ρ_a denotes the gyro-radius of the species a . However, the validity of the second approximation is questioned when E_r takes large positive values [35]. This point will be briefly discussed in section 5.1.

Φ_1 is determined by the quasi-neutrality condition. Imposing the quasi-neutrality condition up to the first order and neglecting n_{e1} yields the expression [22]

$$\begin{aligned} \Phi_1 &= \frac{1}{e} \left(\sum_I Z_I^2 \frac{n_{I0}}{T_I} + \frac{n_{e0}}{T_e} \right)^{-1} \sum_I Z_I n_{I1} \\ &= \frac{1}{e} \left(\sum_I Z_I^2 \frac{n_{I0}}{T_I} + \frac{n_{e0}}{T_e} \right)^{-1} \sum_I Z_I \int d^3v f_{I1}, \end{aligned} \quad (9)$$

where the subscript I refers to ion species.

Time evolution of the ambipolar E_r is determined by

$$\epsilon \frac{\partial E_r}{\partial t} = -e \left(Z_I \sum_I \Gamma_I - \Gamma_e \right), \quad (10)$$

where ϵ is the permittivity [25, 36] and

$$\Gamma_a \equiv \left\langle \int d^3v \dot{\mathbf{X}} \cdot \nabla_r f_{a1} \right\rangle, \quad (11)$$

is the radial particle flux of the species a with $\langle \dots \rangle$ denoting the flux surface average. The numerical treatment of the equation (10) in FORTEC-3D including how to manage with the bifurcation problem is described in [37].

In our global simulations, these quantities are evaluated with the initial condition $f_{a1} = E_r = 0$. The equation for the time evolution of E_r (10) is solved every time step while Φ_1 is updated every certain time steps over which n_{I1} is averaged. The time averaging length is about 1/40 times the collision time.

3.2. Plasma profiles

We investigate three different cases, each corresponding to a different carbon density profile. The n - T profiles, including the carbon density profile, for case A are the same as those used in previous studies on an impurity hole plasma observed in LHD [14, 18, 31]. All of the ion species are assumed to be in thermal equilibrium with each other so that they have the same temperature $T_I = T_i$. That which characterizes an impurity hole plasma and distinguishes it from other ion-root plasmas is its high ion temperature in the core induced by NBI. The radial profiles of the temperatures and densities except for the carbon density profile are plotted in Figure 2.

The carbon density profiles for each case are plotted in Figure 3 and the corresponding profiles of the effective charge $Z_{\text{eff}} \equiv \sum_I n_I Z_I^2 / n_e$ are shown in Figure 4.

For case A, the hollow structure of the carbon density profile is formed at an off-axis region ($0.3 < r/a < 0.7$). The density gradient near the axis thus can contribute

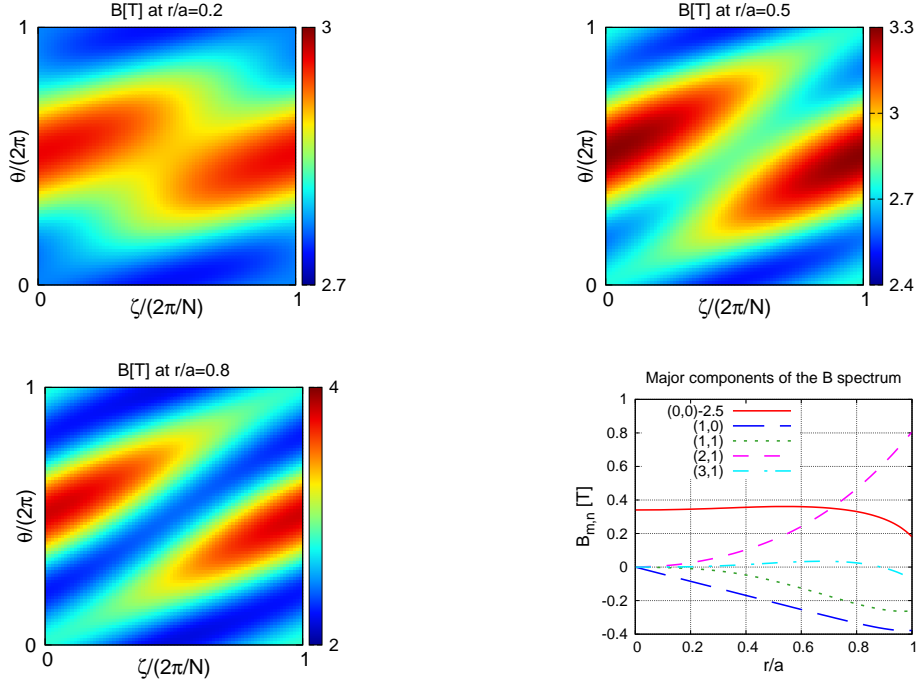


Figure 1. The magnetic field strength on the flux surface at $r/a = 0.2$ (top left), 0.5 (top right) and 0.8 (bottom left), and the major Fourier components of the magnetic field (bottom right). The value of the cosine- $(0, 0)$ component in the bottom right figure is adjusted by subtracting 2.5 for visualization purposes. θ and ζ are the poloidal and the toroidal angles in the Boozer coordinates, respectively, and $N = 10$.

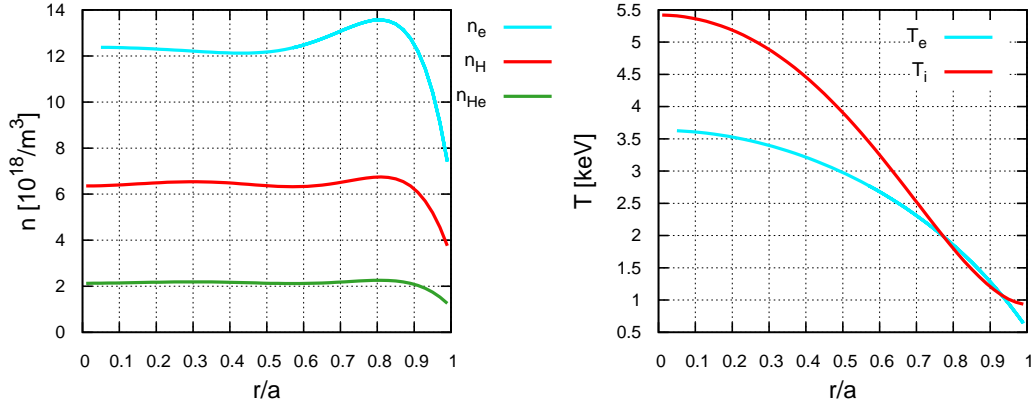


Figure 2. The radial profiles of the densities (left) and temperatures (right) except for the carbon density profile.

to driving the carbon impurities outwardly. Some measurement data, however, indicate that impurity holes are formed around the magnetic axis [11, 12, 13]. For the rest of the cases, the carbon density profile is thus modified to be hollow around the magnetic axis. For case B, the carbon density gradient near the axis is flattened. On the other hand, the gradient near the axis is steepened for case C. Thus, while the density gradient dn_c/dr does not work as a driving force for case B, it works as an inward force for the carbon flux for case C. The carbon impurities in this plasma are in the plateau regime

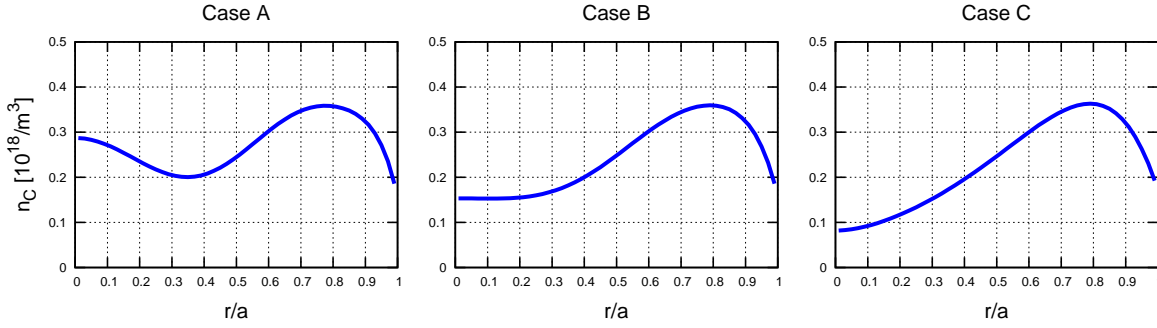


Figure 3. The radial carbon density profiles for case A (left), B (center) and C (right), respectively.

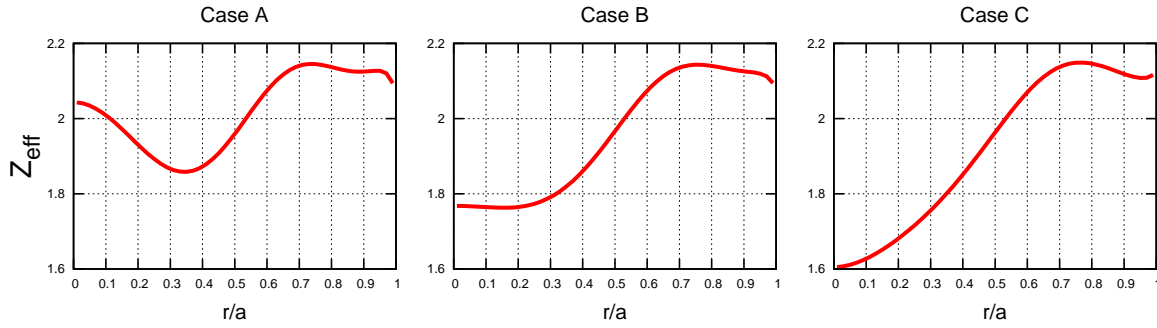


Figure 4. The radial profiles of Z_{eff} for case A (left), B (center) and C (right), respectively.

for the entire radius (see figure 4 in [31]).

In order to preserve the charge-neutrality, the electron density is modified accordingly to the modification in the carbon density profiles as well. However, the differences in the electron density profiles are not explicitly shown because this level of difference can be neglected. The ion and electron temperatures are fixed since it is observed that the changes in the temperatures during phase when the carbon density profile becomes hollower are also small [11, 16, 38].

In order to study the effect of Φ_1 , we simulate the cases with and without Φ_1 for each case.

4. Simulation result

In this section, we present the simulation results of each case. We focus on how and how much the global effects and the Φ_1 -effect give rise to the difference in the ambipolar condition and the radial particle fluxes. Some results of local neoclassical simulation without the Φ_1 -effect by PENTA code are also shown for reference.

4.1. Case A

For case A, the profile of the ambipolar E_r obtained by the global simulation turns out to be quite different from those obtained by local simulations (Figure 5). The

cyan points represent the solution for the case without Φ_1 obtained by using a local code PENTA. The sign of the local solution is negative for almost the entire radius. The local calculation also finds an electron root, represented with blue points, but only partially at $r/a > 0.8$. On the other hand, the sign of the global solutions, which are represented with the red and green lines, is negative near the magnetic axis but transits to positive around $r/a = 0.25$. The red and green lines correspond to the cases with and without Φ_1 , respectively. The solution for a pure plasma, in which the electron density n_e is equal to the hydrogen density n_H , is also shown in Figure 6. By comparing Figure 5 and Figure 6, we find the E_r value is lowered maintaining its profile shape when the impurity contributions are taken into account. The resulting emergence of the ion-root near the axis is a distinctive feature of the simulation result and indicates that the impurity contributions are not negligible in the ambipolar condition.

Compared with the difference between the global solutions, the differences between the global and the local solutions are substantial. However, it is known that the condition of an impurity hole plasma is, even if it were in ion-root, very close to the condition for E_r to be positive [19]. The existence of the positive local solution near the edge suggests that the cause of the difference is more subtle than it looks at a glance. Also, and more crucially, the sign-changing feature is shared with the experimentally observed profile [13] as already mentioned in section 1. Note also that positive E_r in the core region of $T_i > T_e$ discharges have been observed in LHD high- T_i and low- n_e shots [39], where even a local neoclassical code predicts the core electron-root. The difference in shapes of the positive E_r profiles evaluated with FORTEC-3D and PENTA, respectively, at the edge region ($r/a > 0.95$) can be caused by several differences in the models, such as in the orbits and the orbit loss treatments, and in the collision operators. Nevertheless, both codes are designed so that the treatments on the edge boundary do not affect the physics in the inner region.

One may be concerned with the poloidal Mach number $M_p \simeq E_r R_0 / (v_{th} B_0 r \iota)$ for carbon, where B_0 is the magnetic field strength at the magnetic axis, v_{th} is the thermal velocity and ι is the rotational transform, respectively, since nonlinear dependence of the neoclassical poloidal viscosity (and therefore of the radial flux) appears at $|M_p| \simeq 1$, which is caused by the resonance of parallel motion and $E \times B$ rotation [40, 41]. For the ambipolar E_r profile in Figure 5, $|M_p|$ for carbon is $0.2 \sim 0.4$ except for very close to the magnetic axis $r/a < 0.05$, where $|M_p| > 1$. Therefore, the resonance effect is basically irrelevant to the carbon impurity neoclassical flux in the present study.

In Figure 7, the radial particle fluxes of the ion species are plotted. As in Figure 5, the red and green lines correspond to the global calculation results with and without Φ_1 , respectively. For reference, the PENTA results with the ion-root and the electron-root of the ambipolar E_r are also plotted with cyan points and blue points, respectively. Note that the value of the hydrogen flux for the local ion-root case is multiplied by 0.2 for visualization purposes. That is, the original value of the hydrogen flux is five times larger than represented. The reason that the discrepancy in the flux values between the global and local models becomes larger for lighter species is that the impact of the

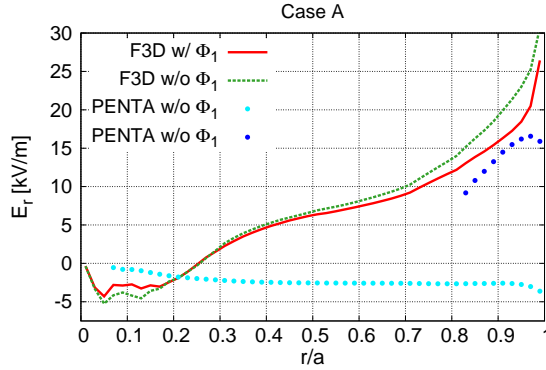


Figure 5. The ambipolar radial electric field profiles for case A. The red and the green lines correspond to the results of FORTEC-3D with and without Φ_1 , and the cyan and the blue points to PENTA results, respectively.

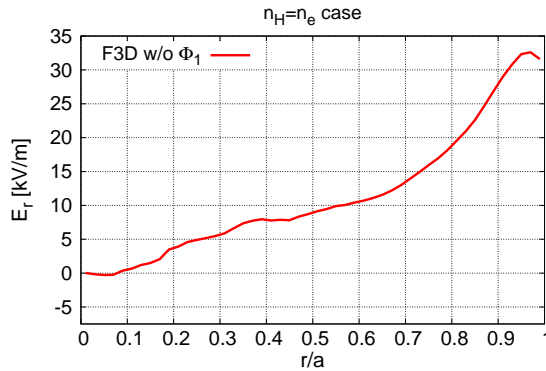


Figure 6. The ambipolar radial electric field profiles obtained by global simulation assuming $n_H = n_e$.

magnetic drift becomes largest for low collisionality regimes [27, 31, 42]. For this case, briefly, the absence of the magnetic drift leads to the overestimation of the $1/\nu$ -type trapped particle diffusion where E_r is close to zero since the particles are stuck in the local helical ripple wells without drift motion. Inclusion of the precession motion of the trapped particles by the magnetic drift significantly moderates the excessive diffusion. The difference in the ambipolar E_r profiles between global and local simulations reflects whether or not the magnetic drift is considered.

As can be seen, regardless of the effect of Φ_1 , all of the ion fluxes are outwardly directed for almost the entire radius. This is the case even for the carbon flux where the sign of E_r is negative ($r/a < 0.25$) and where the carbon density profile is hollow (from $r/a \sim 0.3$ to $r/a \sim 0.7$). The effect of Φ_1 tends to drive the flux more outwardly and its impact is largest for carbon. Therefore, considering the impurity transport in the ambipolar condition increases the portion of the escaping positive charge. The E_r level is consequently lowered as the shift from Figure 6 to Figure 5.

Note that the carbon flux for the local ion-root case is also outwardly directed near the magnetic axis. This is seen in a previous study as well [14]. Remember that for this case, however, the carbon density profile is peaked around the axis. In order for the flux

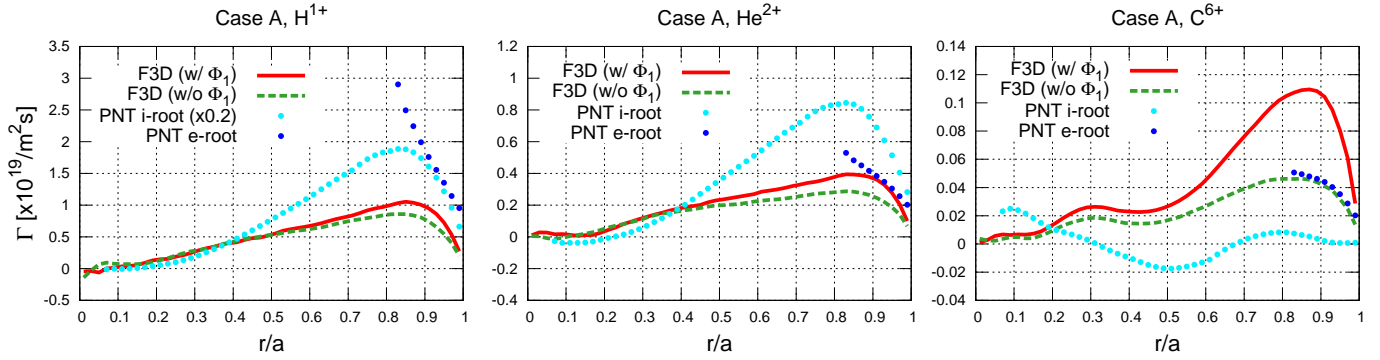


Figure 7. The radial fluxes of H^{1+} (left), He^{2+} (center) and C^{6+} (right) for case A. The red and the green lines correspond to the global calculation results with and without Φ_1 , and the cyan points and the blue points to the PENTA results of the ion-root and the electron-root cases, respectively. Note that the hydrogen flux of the PENTA calculation for the ion-root case is plotted being multiplied by 0.2.

to be consistent with the carbon density profile, the flux should be positive where the hole structure is formed, but this is not the case. To the contrary, the global results are consistent with the density profile as described above.

To be exact, the profile of the turbulent flux, not only the neoclassical flux, is needed to discuss the consistency. Still, the gyrokinetic study has shown that the values of the global neoclassical fluxes of the ion species are close to those to balance with the turbulent fluxes whereas the local neoclassical fluxes are out of balance. The existing data, though still insufficient, are thus in favor of our result on this point as well. We will return to this point in section 5.3.

Figure 8 shows the 2-dimensional spatial structures of Φ_1 and the carbon density variation n_{C1} on the flux surfaces at $r/a = 0.1, 0.2, 0.3$ and 0.4 , respectively. θ and ζ are the poloidal and the toroidal angles of the Boozer coordinates, respectively, and N is the toroidal symmetry number ($N = 10$ for LHD). The poloidal angle θ is chosen to be zero on the outboard side. The phase of Φ_1 , which is mainly determined by the phase of the hydrogen density variation n_{H1} , is stellarator symmetric while the phase of carbon density appears to be stellarator anti-symmetric. These results are consistent with analytical estimation of the collisionality dependence of the size and the phase of density variation, and therefore of Φ_1 [43, 44]. The structural difference in the density variations can roughly be argued by a criterion known for classical stellarators as well. When the poloidal precession frequency $\Omega_\theta \simeq \Omega_E \simeq E_r/(rB_{00})$ exceeds the effective collision frequency ν_{eff} , the $\cos\theta$ component becomes the leading mode in the spatial distribution. On the other hand, as $\nu_{\text{eff}}/\Omega_\theta$ increases, the $\sin\theta$ component grows relatively larger [22, 45]. For this case, $\nu_{\text{eff}}/\Omega_\theta \sim O(1)$ for carbon while $\nu_{\text{eff}}/\Omega_\theta \sim O(0.1)$ for hydrogen and helium.

Among the presented figures, the amplitude of both Φ_1 and n_{C1} become minimum at $r/a = 0.2$, which is a position close to the transition point of E_r . Also, the structure of Φ_1 on the surface at $r/a = 0, 2$ is rather disordered compared with those on the other

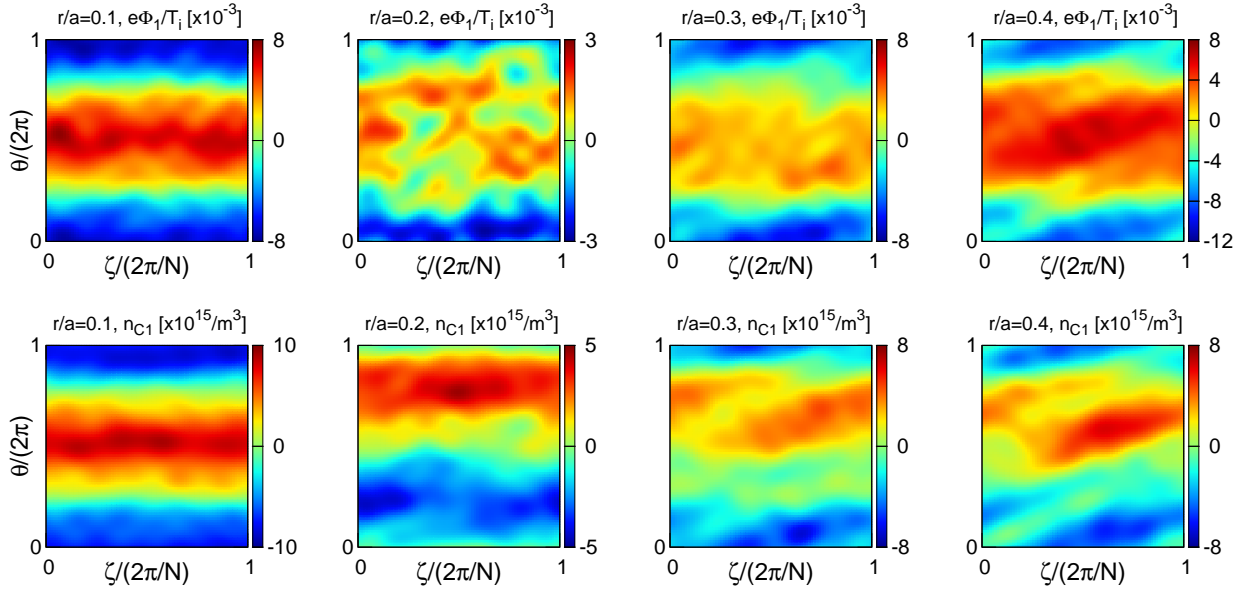


Figure 8. The spatial structures of Φ_1 (the upper figures) and n_{C1} (the lower figures) for case A. From left to right, each column corresponds to the flux surface at $r/a = 0.1, 0.2, 0.3$ and 0.4 , respectively.

surfaces. Figure 9 shows this in terms of the Fourier spectrum. The left figure is the radial profile of the Φ_1 spectrum. As can be seen, the leading mode, $\cos(1, 0) = \cos \theta$, is shrunk around $r/a = 0.2$ and no single specific mode becomes dominant there. The center figure shows the spectrum of

$$\bar{v}_{E1} \equiv \sqrt{g} \mathbf{v}_{E1} \cdot \nabla r, \quad (12)$$

where \sqrt{g} is the Jacobian and \mathbf{v}_{E1} is the $E \times B$ -drift generated by Φ_1 . Not \mathbf{v}_{E1} itself but \bar{v}_{E1} is plotted since the radial particle flux driven by \mathbf{v}_{E1} can be calculated by the sum of the products of the Fourier coefficients of \bar{v}_{E1} and n_{a1} [31]. Since $\mathbf{v}_{E1} \cdot \nabla r$ is given by a derivative of Φ_1 , the $\sin(1, 0) (= \sin \theta)$ mode becomes one of the dominant modes in the \bar{v}_{E1} spectrum. As shown in the right figure, this mode becomes dominant in the n_{C1} spectrum at $r/a > 0.2$ as well. The coupling of this mode with the same sign between \bar{v}_{E1} and n_{C1} results in the outward enhancement of the carbon flux at outer radii (see Figure 7).

4.2. Case B

The realization of the outward carbon flux near the axis for case A is not so surprising since the carbon density gradient at the region is negative, which works as an outward driving force, and the E_r takes positive value where the density gradient is no longer negative. For case B, the outward driving force is removed by flattening the carbon density profile near the axis. Let us see how the behaviors of the carbon impurities respond to this modification.

The ambipolar E_r profile for case B is close to that for case A (Figure 10). The E_r thus contributes to driving the ion fluxes inwardly near the axis. Further, unlike case

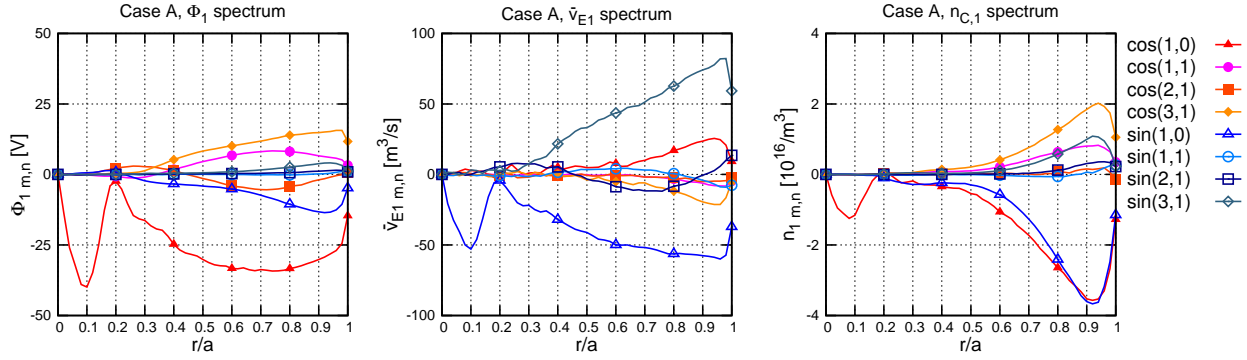


Figure 9. The radial profiles of the leading modes in the Fourier spectra of Φ_1 (left), \bar{v}_{E1} (center) and n_{C1} for case A, respectively.

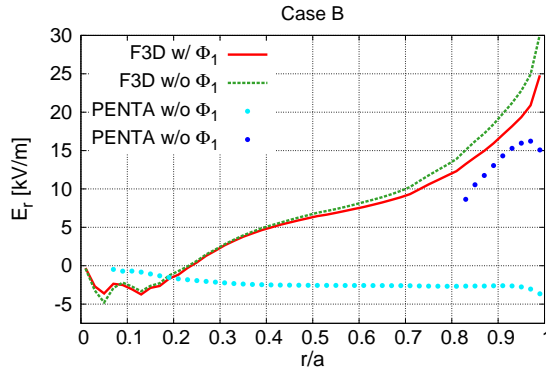


Figure 10. The ambipolar radial electric field profiles for case B. The red and the green lines correspond to the results of FORTEC-3D with and without Φ_1 , and the cyan and the blue points to PENTA results, respectively.

A, the carbon density gradient near the axis is flat for this case. As a consequence, the carbon flux without Φ_1 is slightly negative around $0.1 < r/a < 0.2$ though its absolute value is close to zero as shown in Figure 11. However, when Φ_1 is taken into account, the flux is driven outwardly for the entire radius. The flux profiles of the other ion species are very similar to those for case A. As shown in the analysis of [15, 19], the outward contribution of the ion temperature gradient to the carbon flux can be comparable with the inward contribution of the negative but small E_r in high- T_i plasmas. The almost zero carbon flux near the axis for the case without Φ_1 manifests this feature.

The reason for the outward enhancement of the carbon flux can be seen in the structures of Φ_1 and n_{C1} (Figure 12) and their Fourier spectra (Figure 13). While the Φ_1 spectrum, and therefore the \bar{v}_{E1} spectrum, for this case are similar to those for case A, a subtle difference in the n_{C1} spectrum can be seen. The $\sin(1,0)$ mode in the n_{C1} spectrum starts growing around $r/a = 0.1$ and couples with the same mode in the \bar{v}_{E1} spectrum. In fact, although it is too small to see in the figure, the $\sin(1,0)$ mode takes finite negative values near the axis as well. The $\sin(1,0)$ mode with the negative sign is also a leading mode in the radial magnetic drift $\mathbf{v}_m \cdot \nabla r$. These couplings result in the outward carbon flux for the entire radius.

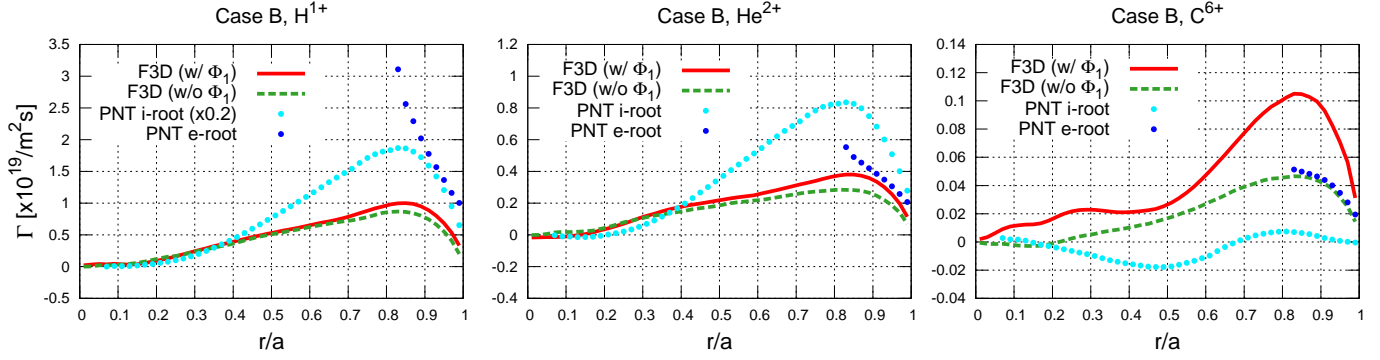


Figure 11. The radial fluxes of H^{1+} (left), He^{2+} (center) and C^{6+} (right) for case B. The red and green lines correspond to the global calculation results with and without Φ_1 , and the cyan points and the blue points to the PENTA results of the ion-root and the electron-root cases, respectively. Note that the hydrogen flux of the PENTA calculation for the ion-root case is plotted being multiplied by 0.2.

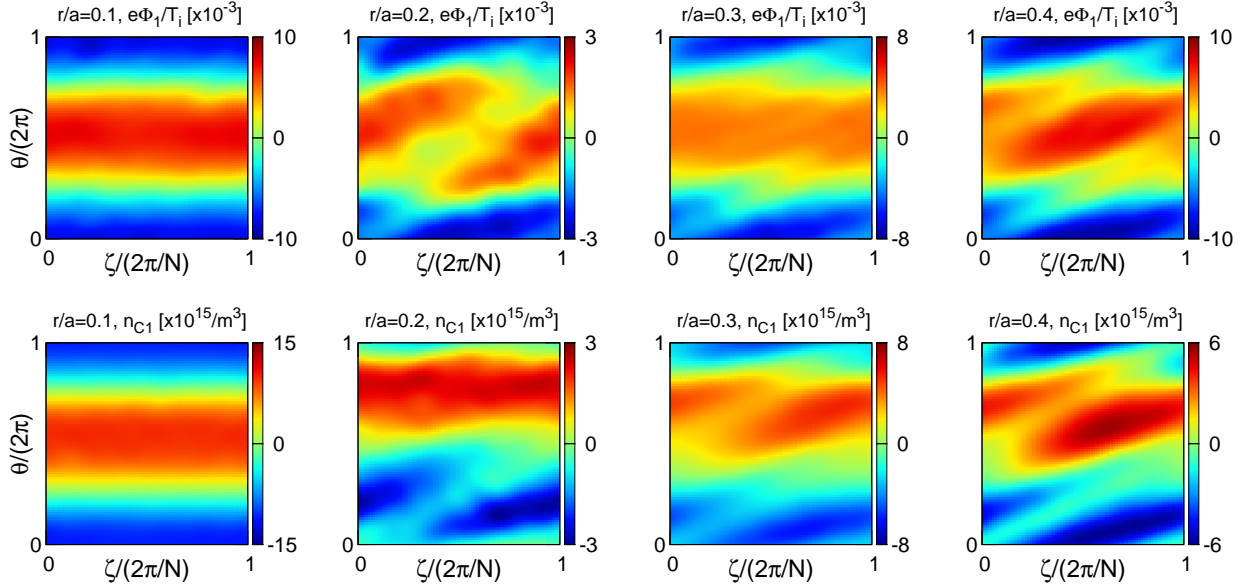


Figure 12. The spatial structures of Φ_1 (the upper figures) and n_{C1} (the lower figures) for case B. From left to right, each column corresponds to the flux surface at $r/a = 0.1, 0.2, 0.3$ and 0.4 , respectively.

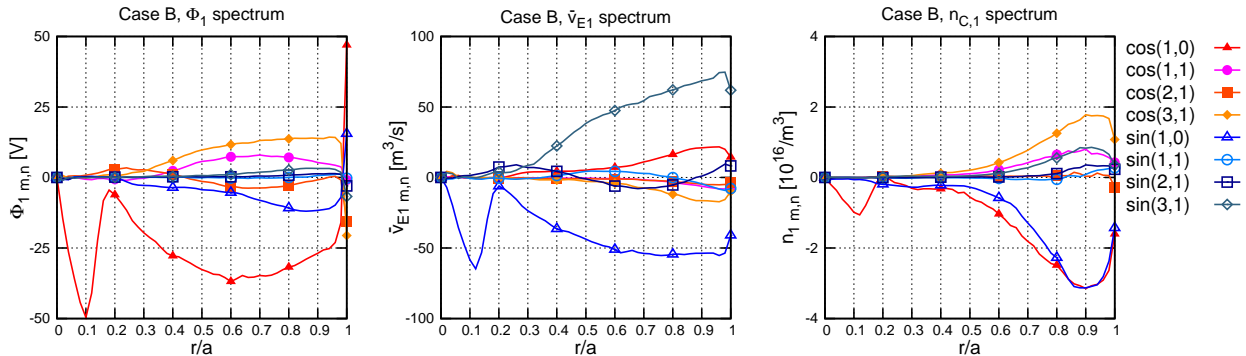


Figure 13. The radial profiles of the leading modes in the Fourier spectra of Φ_1 (left), \bar{v}_{E1} (center) and n_{C1} for case B, respectively.

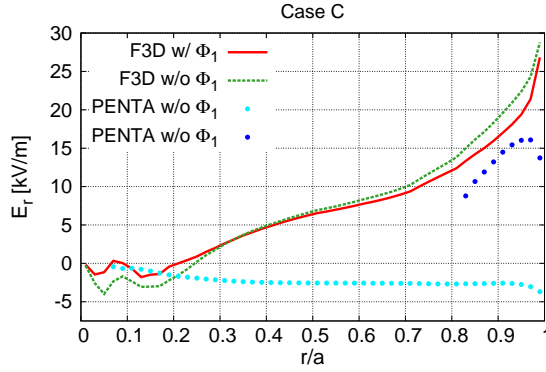


Figure 14. The ambipolar radial electric field profiles for case C. The red and the green lines correspond to the results of FORTEC-3D with and without Φ_1 , and the cyan and the blue points to PENTA results, respectively.

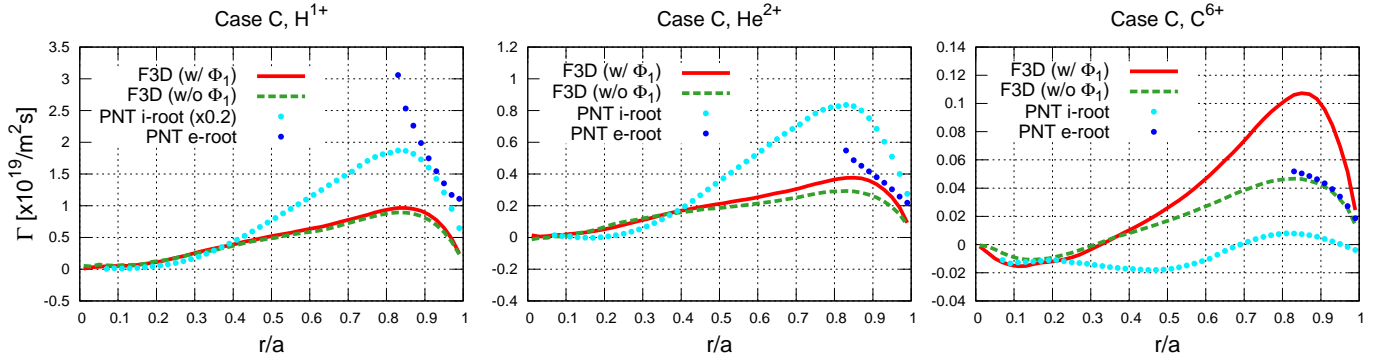


Figure 15. The radial fluxes of H^{1+} (left), He^{2+} (center) and C^{6+} (right) for case C. The red and green lines correspond to the global calculation results with and without Φ_1 , and the cyan points and the blue points to the PENTA results of the ion-root and the electron-root cases, respectively. Note that the hydrogen flux of the PENTA calculation for the ion-root case is plotted being multiplied by 0.2.

4.3. Case C

For case B, we saw that the carbon flux near the axis can be outwardly directed even where $dn_C/dr \sim 0$ and $E_r < 0$. For case C, the carbon density gradient is further steepened and rendered to have positive values.

The ambipolar E_r profile for case C without Φ_1 is qualitatively analogous to those for the first two cases. However, when Φ_1 is included, the value of E_r is shifted to be close to zero near the axis (Figure 14).

In Figure 15, the radial profiles of the ion particle fluxes are represented. The hydrogen and helium fluxes are also similar to those for the previous two cases and are insensitive to the change in the E_r profile near the axis due to Φ_1 . In contrast, the carbon flux near the axis is inwardly directed whether or not Φ_1 is included. This indicates that the steep gradient of the carbon density becomes a dominant driving force for the carbon flux. Also, unlike the previous two cases, Φ_1 contributes to driving the carbon flux more inwardly.

This inward enhancement is also caused by the coupling of the $\sin(1,0)$ mode.

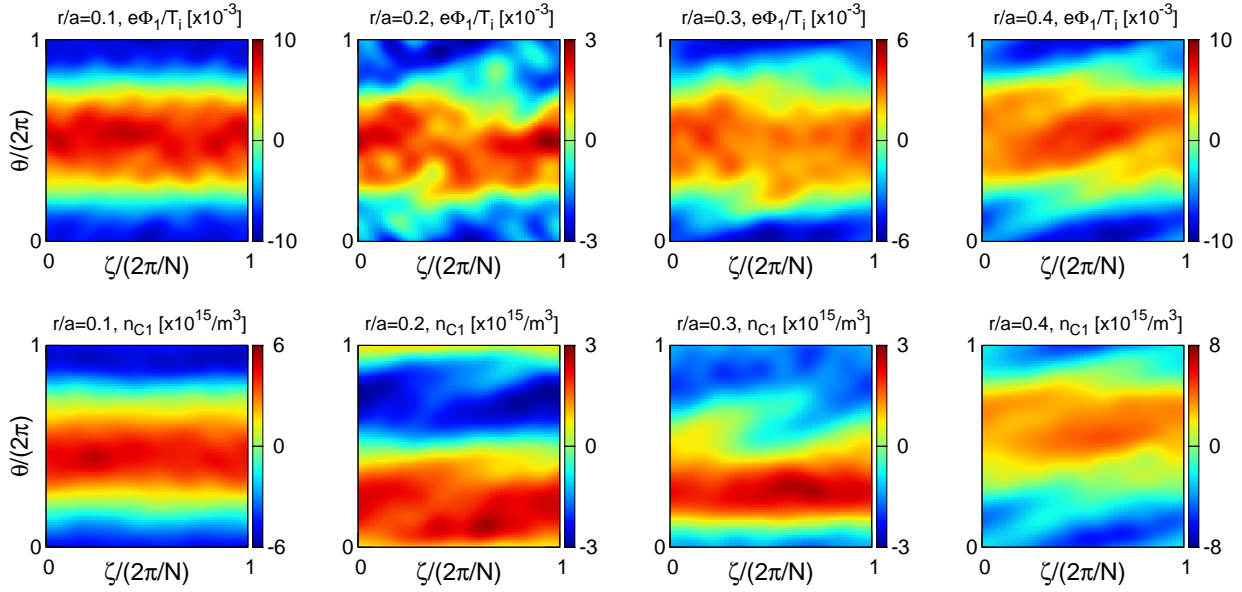


Figure 16. The spatial structures of Φ_1 (the upper figures) and n_{C1} (the lower figures) for case C. From left to right, each column corresponds to the flux surface at $r/a = 0.1, 0.2, 0.3$ and 0.4 , respectively.

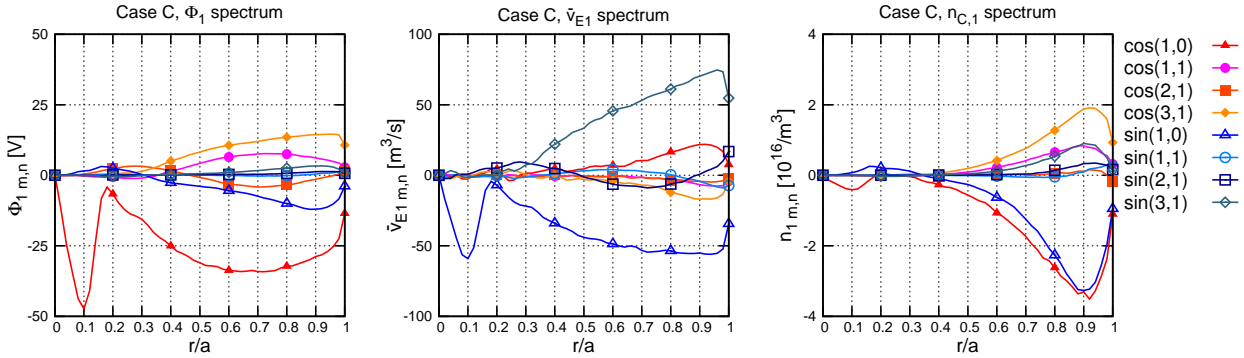


Figure 17. The radial profiles of the leading modes in the Fourier spectra of Φ_1 (left), \bar{v}_{E1} (center) and n_{C1} for case C, respectively.

The spatial structures of Φ_1 and n_{C1} are represented by Figure 16. By comparing the n_{C1} structure at $r/a = 0.2$ with that for case B (Figure 12), it can be seen that the distribution of the carbon impurities is inverted in θ -direction. This reflects the fact that the sign of the $\sin(1,0)$ mode at $r/a < 0.3$ for this case is opposite from that for case B (Figure 17). This inversion results in the opposite-sign coupling between \bar{v}_{E1} and n_{C1} and leads to the inward enhancement of the carbon flux near the axis.

5. Summary and discussion

5.1. Global effects and ambipolar radial electric field profile

By global simulation, we found the solutions of the ambipolar condition which change the sign from negative to positive along the minor radius. With such E_r , the impurity

carbon flux can be outwardly directed even where $E_r < 0$ and the carbon density profile is hollow. The root-transitioning has been experimentally observed in an impurity hole plasma and our result is thus qualitatively consistent with the experiment. However, several tasks and challenges still remain to reveal the mechanism behind the impurity hole formation.

By global neoclassical simulation, a radially continuous profile of ambipolar E_r and of the corresponding neoclassical fluxes can be obtained even when the E_r changes its sign. By local simulation, on the other hand, the connection between an ion root and an electron root cannot be determined by itself. To determine how to connect the two different roots by local simulation, the finite-orbit-width (FOW) effect or the effects of anomalous transport on the radial fluxes need to be modelled and incorporated into the simulation model [46, 47]. The resulting E_r profile generally shows a transition within a very small radial range ($\Delta r/a \ll 0.1$) having a large slope across the transitioning surface [48, 49] because the neoclassical hydrogen flux is overestimated in the limit $E_r \rightarrow 0$. In the measurement of [13], however, the transition width appears to be $\Delta r/a = 0.1 \sim 0.2$. This size is of the same scale as the typical ion drift orbit width and thus qualitatively consistent with our present simulation result in which the FOW effect is included *per se*. Therefore, if the transition of the E_r sign is a fundamental property of impurity hole plasmas, a global code which essentially includes the FOW effect has an advantage over local codes. Still, it has been shown that the local neoclassical models retaining the tangential magnetic drift can yield results close to those of the global calculations of FORTEC-3D [27, 30, 42, 50]. Compared with the relative largeness of the computational cost of global simulation to that of local simulation, the additional computational cost required to include the tangential magnetic drift in a local code is not significant. Thus, if the local codes retaining tangential magnetic drift can provide reliable estimations of the quantities we are interested in, namely ambipolar E_r , Φ_1 , and the neoclassical fluxes in impurity hole plasmas except for the neighborhood of the surface where $E_r = 0$, the modified local-models also become useful tools to investigate the impurity hole phenomenon. In particular, the models can be used to perform parameter surveys such as to analyze the dependence of the phenomenon on the n - T profiles or on the magnetic field configuration. To assess this point, we first need to understand how inclusion of the magnetic drift works precisely and to what extent the global effects are necessary by comparing simulation results of the global and local models with tangential magnetic drift.

The discrepancy of the transitioning points between the numerical results and the experimental data is also to be examined. The radial domain where $E_r < 0$ is roughly $r/a < 0.25$ in the numerical results while $r/a < 0.55$ in the experimental data. Since our plasma profiles are not the same as those of the experimentally studied plasma, the transitioning points need not coincide with each other exactly. However, it is not clear if the carbon flux would still be outwardly directed when the negative- E_r region is expanded in numerical simulation.

Disagreement in the ambipolar E_r profiles suggests the possibility that we still lack

some essential factors to determine the ambipolar condition. If so, the impact of NBI heating is one of the candidates for it is shown that an NBI can change the E_r profile [20, 51]. In fact, the impurity holes in LHD are usually formed after the tangential NBI is applied. It is also worthwhile examining the effect of NBI fast-ion anisotropic distribution on the Φ_1 potential profile [52] in the impurity hole plasmas. The effect of NBI fast-ion on neoclassical and turbulent transport has also been studied to explain the hollow impurity density profiles observed in tokamaks [53]. In order to verify these effects, our numerical model needs to be enabled to incorporate the impact of NBI.

To evaluate the ambipolar E_r and Φ_1 in the present study, the local approximation and adiabatic response to Φ_1 have been adopted for electrons, since solving the electron distribution function as well as the ions distribution functions by the global drift-kinetic model is much too time-consuming. Though the local approximation for electron neoclassical transport is thought to be more accurate than for ions, it has been demonstrated that the discrepancy between local and global electron fluxes Γ_e in LHD can become considerable as the electron collisionality becomes lower [26]. The finite magnetic drift changes the E_r dependence of Γ_e as well as the main ion flux Γ_i in low-collisionality plasmas and will result in different E_r profile from the simulation which uses local Γ_e . In a study using local neoclassical model, non-adiabatic, kinetic treatment of electrons in the evaluation of Φ_1 potential has been shown to be more important in electron-root than in ion-root [35]. Although our main focus is on the near-axis region where only ion-root is found, the study shows the contribution of the kinetic electrons to Φ_1 also becomes large where the root-transitioning occurs and $-d\Phi_1/dr$ exhibits an appreciable value on the transitioning surface. The absolute value of $-d\Phi_1/dr$ is not very large (at most, 1 keV/m), but the contribution cannot be ignored to determine the exact position where the total radial electric field changes its sign. However, predictions of local models for low-collisionality plasmas can be inaccurate especially when E_r is close or equal to zero, as has been mentioned throughout this article. It is an open question whether the tendency found in the local but kinetic electron simulation holds true in global simulation or not.

5.2. Impact of Φ_1

In the present study, we found that the impact of Φ_1 on the ambipolar radial electric field and particle fluxes of light ion species (H^{1+} and He^{2+}) are insignificant. On the contrary, as was most remarkable for case B, it was shown that Φ_1 does play a role in the transport of carbon impurities and can be non-negligible. However, when the impurity flux is inwardly directed and its value is sufficiently large as that for case C, Φ_1 contributes to driving the impurity flux further inwardly.

This tendency of Φ_1 to contribute to enhancing the absolute value of carbon flux and not to invert the sign of the flux was found in our previous study as well [31]. That is, Φ_1 drives the flux more outwardly if the flux is outwardly directed without Φ_1 but it drives the flux more inwardly if the flux is inwardly directed without Φ_1 . Whether

Φ_1 drives the flux inward or outward depends on the spectrum structures of the density variation and Φ_1 . Even if the contribution of kinetic electrons turns out to be non-negligible for some aspects under the plasma condition we have considered, it cannot be expected that the impact will be so large as to turn the spectrum structure of Φ_1 determined by ions upside down. Thus, Φ_1 cannot solely fill the gap between the experimental observations and the conventional neoclassical analysis. This fact suggests that the global drift-kinetic model is one of the fundamental keys to explain the formation of an impurity hole, where the inward impurity turbulent flux should be balanced with the outward neoclassical flux, as we will discuss below.

5.3. Consistency between the particle fluxes and density profiles

By comparing the results of cases A to C, we can infer the process of an impurity hole formation. As long as the carbon density profile near the magnetic axis is not hollow as in case A or moderately hollow as in case B, the carbon flux near the axis can be outwardly directed. Neglecting the impurity particle source and turbulent transport, our neoclassical simulation results then mean that carbon density near the axis continues to decrease and the density gradient becomes steeper accordingly. When the gradient becomes as steep as that for case C, the direction of the carbon flux inverts. This suggests the process that the radial particle fluxes are balanced between the states corresponding to cases B and C, and the steady density profile is achieved there.

The density profile is determined by the particle balance equation

$$\frac{\partial n_a}{\partial t} + \frac{1}{V'} \frac{d}{dr} (V' \Gamma_a^{\text{tot}}) = S_a, \quad (13)$$

where S_a is a source term, V' is the radial derivative of the volume enclosed by the flux surface r and the total radial particle flux Γ_a^{tot} is given by the sum of the neoclassical contribution Γ_a^{NC} and the turbulent contribution Γ_a^{Trb} :

$$\Gamma_a^{\text{tot}} = \Gamma_a^{\text{NC}} + \Gamma_a^{\text{Trb}}. \quad (14)$$

In the impurity hole discharge in LHD analyzed here, a particle source of carbon in the plasma core region existed only in an instant when a carbon pellet was injected [16]. Figure 5 in [16] also shows that the impurity hole is a transition phenomenon in which the hollow C^{6+} density decays in time. The time scale of density decay is estimated as $\tau_{\text{decay}} = [\partial(\ln n_C)/\partial t]^{-1} \sim O(0.1\text{s})$ from the figure. On the other hand, in the FORTEC-3D simulations, the ambipolar condition was achieved in $10\tau_c \sim 0.001\text{s}$ where τ_c is the collision time of carbon, which is a much shorter time scale than τ_{decay} . Therefore, we can analyze the particle balance in the impurity hole plasma by approximating $\partial n_c/\partial t = S_c \simeq 0$ in eq.(13).

For a steady state without a particle source, the neoclassical and the turbulent contributions must cancel each other so that the total flux vanishes. The particle flux we have investigated in this article is only the neoclassical part and we thus cannot make a rigorous argument about whether the obtained profiles of the carbon flux and the carbon density are consistent. Nevertheless, an existing literature is in favor of

our result. The study [18] has investigated both the local neoclassical and ITG-driven turbulent fluxes in impurity hole plasmas by using a nonlinear gyrokinetic simulation code GKV. It is shown in the study that the value of the ambipolar E_r should be positive at least around $0.52 < r/a < 0.61$ for both contributions of the fluxes to balance each other.

It was shown in the study that the carbon nonlinear turbulent flux on the surfaces at $r/a = 0.52$ and $r/a = 0.61$, where the hollow n_C profile is formed, are always negative in spite of a wide range scan of local carbon density and temperature gradients around the nominal values of them in case A. The inward pinch of impurity turbulent flux was also predicted in a quasilinear estimation previously [16]. In [18], it was conjectured that Γ_C^{NC} on the flux surface where the impurity hole is formed should be positive for some reason so as to balance with negative Γ_C^{Trb} . The authors of the study pointed out that E_r and Γ_C^{NC} (from local model) can become positive by the effect of tangential NBI torque. In the present study, we found that the positive E_r and Γ_C^{NC} appear as solutions of global neoclassical transport simulation.

Figure 18 compares the $-\Gamma_a^{\text{NC}}$ calculated with PENTA and with FORTEC-3D in this work, respectively against Γ_a^{Trb} obtained with a local gyrokinetic code GKV in [18] at $r/a = 0.52$ and $r/a = 0.61$. All the calculations are done using the same n - T profiles which correspond to those for case A in this work. Except for the FORTEC-3D calculation, Φ_1 is not considered. As shown in section 4.1, PENTA finds an ion-root while FORTEC-3D finds an electron-root in the region considered here. The gyrokinetic simulation assumes that the turbulent transport is independent of E_r . The helium flux and the carbon flux are plotted being multiplied by 10 and 30, respectively, for visualization purposes. The first point to note is that, as has been discussed, the signs of the neoclassical carbon flux predicted by the PENTA (left column) and the FORTEC-3D (center column) simulations are opposite. Only the global $-\Gamma_C^{\text{NC}}$ has the same sign as Γ_C^{Trb} (right column) and they are only a factor 2 to 3 from being balanced. On the other hand, both local and global simulations predict the opposite sign for $-\Gamma_{\text{He}}^{\text{NC}}$ from that of $\Gamma_{\text{He}}^{\text{Trb}}$ though the global result is closer to the turbulent contribution than the local result is. The largest discrepancy in the absolute value is seen in the hydrogen fluxes. While the FORTEC-3D result is close to that of the GKV result, the PENTA result is far from balancing with the turbulent counterpart. Therefore, in terms of the carbon and hydrogen flux balance, the scenario in which $E_r > 0$ at least at $r/a > 0.5$ is more plausible than the conventional ion-root scenario. The study [18] reaches the same conclusion by comparing the turbulent fluxes with the local neoclassical fluxes for an electron-root case as well as with the ion-root case considered here.

It is to be noted that the turbulent fluxes show “stiffness” and are much more susceptible to changes in the local density and temperature gradients than neoclassical fluxes are. In figure 4 of [18], the turbulent electron and ion energy fluxes from gyrokinetic simulation were compared with their experimental observation values. The simulation and observation values match if the T_i gradient scale length is reduced by only about 30% from the nominal value. If we admit the “flux-matching” condition [54]

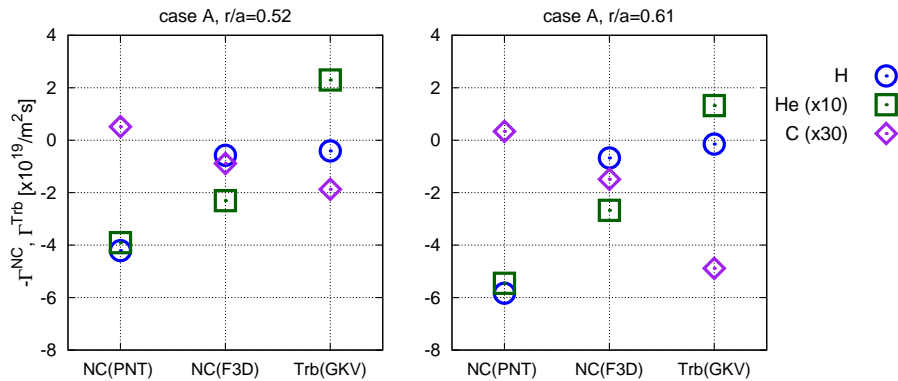


Figure 18. Comparisons of $-\Gamma_a^{\text{NC}}$ obtained with PENTA (left) and with FORTEC-3D (center), respectively and Γ_a^{Trb} obtained with GKV in [18] (right). Note that the values of the helium flux and the carbon flux are being multiplied by 10 and 30, respectively, for visualization purposes. The left figure shows the comparison on the flux surface at $r/a = 0.52$ and the right figure at $r/a = 0.61$, respectively.

to explain the disagreement between observed and calculated energy fluxes by means of the ambiguity in the local temperature gradient, Γ_C^{Trb} can then be reestimated by gyrokinetic simulation at the energy flux-matched temperature gradients of electrons and ions. Indeed, it is confirmed that the energy flux-matched Γ_C^{Trb} tends to be much in close balance with Γ_C^{NC} obtained by the global neoclassical simulation with Φ_1 [55, 56]. In addition, with the modified temperature gradient, the turbulent helium flux is reduced by about one-half, while hydrogen flux remains almost unchanged. Thus, considering the flux-matching of turbulent energy transport gives better particle balance $\Gamma_a^{\text{NC}} + \Gamma_a^{\text{Trb}} \simeq 0$ for each particle species. Our result thus can be added to the agreement between the experimental and the numerical studies. Nevertheless, further investigation on the flux balance using some sorts of integrated models of neoclassical and turbulent transport, especially for the near-axis region, is necessary to make a more precise argument.

In summary, by global simulation, we reproduced the ambipolar E_r which changes its sign along the minor radius and the outward neoclassical carbon flux. These are two aspects of impurity hole plasmas observed by experiments but have not been captured by local neoclassical simulations. Also, the neoclassical and the turbulent particle fluxes nearly balance with each other which can explain the particle balance in the impurity hole plasma.

Acknowledgments

This work is performed under the auspices of the NIFS Collaborative Research Program, No. NIFS18KNST132. The simulations in this article were carried out on Plasma Simulator in NIFS, Japan and on JFRS-1 supercomputer system at Computational Simulation Centre of International Fusion Energy Research Centre (IFERC-CSC) in Rokkasho Fusion Institute of QST (Aomori, Japan).

References

- [1] D. D.-M. Ho and R. M. Kulsrud. Neoclassical transport in stellarators. *The Physics of Fluids*, 30(2):442–461, 1987.
- [2] H. Maaßberg, C. D. Beidler, and E. E. Simmet. Density control problems in large stellarators with neoclassical transport. *Plasma Physics and Controlled Fusion*, 41(9):1135, 1999.
- [3] S. P. Hirshman. Transport properties of a toroidal plasma in a mixed collisionality regime. *The Physics of Fluids*, 19(1):155–158, 1976.
- [4] P. Helander, S. L. Newton, A. Mollén, and H. M. Smith. Impurity transport in a mixed-collisionality stellarator plasma. *Physical review letters*, 118(15):155002, 2017.
- [5] S. L. Newton, P. Helander, A. Mollén, and H. M. Smith. Impurity transport and bulk ion flow in a mixed collisionality stellarator plasma. *Journal of Plasma Physics*, 83(5), 2017.
- [6] I. Calvo, F. I. Parra, J. L. Velasco, J. A. Alonso, and J. M. García-Regaña. Stellarator impurity flux driven by electric fields tangent to magnetic surfaces. *Nuclear Fusion*, 58(12):124005, 2018.
- [7] S. Buller, H. M. Smith, P. Helander, A. Mollén, S. L. Newton, and I. Pusztai. Collisional transport of impurities with flux-surface varying density in stellarators. *Journal of Plasma Physics*, 84(4), 2018.
- [8] M. F. Martin and M. Landreman. Impurity temperature screening in stellarators close to quasisymmetry. *Journal of Plasma Physics*, 86(3):905860317, 2020.
- [9] I. Calvo, F. I. Parra, J. L. Velasco, and J. M. García-Regaña. Impact of main ion pressure anisotropy on stellarator impurity transport. *Nuclear Fusion*, 60(1):016035, 2020.
- [10] R. Burhenn, Y. Feng, K. Ida, H. Maassberg, K. J. McCarthy, D. Kalinina, M. Kobayashi, S. Morita, Y. Nakamura, H. Nozato, S. Okamura, S. Sudo, C. Suzuki, N. Tamura, A. Weller, M. Yoshinuma, and B. Zurro. On impurity handling in high performance stellarator/heliotron plasmas. *Nuclear Fusion*, 49(6):065005, 2009.
- [11] K. Ida, M. Yoshinuma, M. Osakabe, K. Nagaoka, M. Yokoyama, H. Funaba, C. Suzuki, T. Ido, A. Shimizu, I. Murakami, et al. Observation of an impurity hole in a plasma with an ion internal transport barrier in the Large Helical Device. *Physics of Plasmas*, 16(5):056111, 2009.
- [12] M. Yoshinuma, K. Ida, M. Yokoyama, M. Osakabe, K. Nagaoka, S. Morita, M. Goto, N. Tamura, C. Suzuki, S. Yoshimura, et al. Observation of an impurity hole in the Large Helical Device. *Nuclear Fusion*, 49(6):062002, 2009.
- [13] T. Ido, A. Shimizu, M. Nishiura, K. Nagaoka, M. Yokoyama, K. Ida, M. Yoshinuma, K. Toi, K. Itoh, H. Nakano, et al. Experimental study of radial electric field and electrostatic potential fluctuation in the Large Helical Device. *Plasma Physics and Controlled Fusion*, 52(12):124025, 2010.
- [14] A. Mollén, M. Landreman, H. M. Smith, J. M. García-Regaña, and M. Nunami. Flux-surface variations of the electrostatic potential in stellarators: impact on the radial electric field and neoclassical impurity transport. *Plasma Physics and Controlled Fusion*, 60(8):084001, 2018.
- [15] J. L. Velasco, I. Calvo, J. M. García-Regaña, F. I. Parra, S. Satake, J. A. Alonso, and the LHD team. Large tangential electric fields in plasmas close to temperature screening. *Plasma Physics and Controlled Fusion*, 60(7):074004, 2018.
- [16] D. R. Mikkelsen, K. Tanaka, M. Nunami, T-H. Watanabe, H. Sugama, M. Yoshinuma, K. Ida, Y. Suzuki, M. Goto, S. Morita, et al. Quasilinear carbon transport in an impurity hole plasma in lhd. *Physics of Plasmas*, 21(8):082302, 2014.
- [17] M. Nunami, H. Sugama, J. L. Velasco, M. Yokoyama, M. Sato, M. Nakata, and S. Satake. Anomalous and neoclassical transport of hydrogen isotope and impurity ions in LHD plasmas. In *26th IAEA FEC TH/P2-3*, 2016.
- [18] M. Nunami, M. Nakata, S. Toda, and H. Sugama. Gyrokinetic simulations for turbulent transport of multi-ion-species plasmas in helical systems. *Physics of Plasmas*, 27(5):052501, 2020.
- [19] J. L. Velasco, I. Calvo, S. Satake, A. Alonso, M. Nunami, M. Yokoyama, M. Sato, T. Estrada, J. M. Fontdecaba, M. Liniers, et al. Moderation of neoclassical impurity accumulation in high

- temperature plasmas of helical devices. *Nuclear Fusion*, 57:016016, 2017.
- [20] M. Nunami, M. Sato, M. Nakata, S. Toda, H. Sugama, M. Yokoyama, and H. Yamaguchi. Impacts of external momentum torque on impurity particle transport in LHD. *Plasma and Fusion Research*, 12:1203039–1203039, 2017.
- [21] J. M. García-Regaña, R. Kleiber, C. D. Beidler, Y. Turkin, H. Maaßberg, and P. Helander. On neoclassical impurity transport in stellarator geometry. *Plasma Physics and Controlled Fusion*, 55(7):074008, 2013.
- [22] J. M. García-Regaña, C. D. Beidler, R. Kleiber, P. Helander, A. Mollén, J. A. Alonso, M. Landreman, H. Maaßberg, H. M. Smith, Y. Turkin, and J. L. Velasco. Electrostatic potential variation on the flux surface and its impact on impurity transport. *Nuclear Fusion*, 57(5):056004, 2017.
- [23] K. Nagaoka, K. Ida, M. Yoshinuma, Y. Takeiri, M. Yokoyama, S. Morita, K. Tanaka, T. Ido, A. Shimizu, N. Tamura, et al. Heat and momentum transport of ion internal transport barrier plasmas on the Large Helical Device. *Nuclear Fusion*, 51(8):083022, 2011.
- [24] S. Satake, M. Okamoto, N. Nakajima, H. Sugama, M. Yokoyama, and C. D. Beidler. Non-local neoclassical transport simulation of geodesic acoustic mode. *Nuclear fusion*, 45(11):1362, 2005.
- [25] S. Satake, Yasuhiro Idomura, Hideo Sugama, and T-H Watanabe. Benchmark test of drift-kinetic and gyrokinetic codes through neoclassical transport simulations. *Computer Physics Communications*, 181(6):1069–1076, 2010.
- [26] S. Matsuoka, S. Satake, M. Yokoyama, A. Wakasa, and S. Murakami. Neoclassical electron transport calculation by using δf Monte Carlo method. *Physics of Plasmas*, 18(3):032511, 2011.
- [27] S. Matsuoka, S. Satake, R. Kanno, and H. Sugama. Effects of magnetic drift tangential to magnetic surfaces on neoclassical transport in non-axisymmetric plasmas. *Physics of Plasmas*, 22(7):072511, 2015.
- [28] B. Huang, S. Satake, R. Kanno, H. Sugama, and S. Matsuoka. Benchmark of the local drift-kinetic models for neoclassical transport simulation in helical plasmas. *Physics of Plasmas*, 24(2):022503, 2017.
- [29] S. Satake, M. Nakata, T. Pianpanit, H. Sugama, M. Nunami, S. Matsuoka, S. Ishiguro, and R. Kanno. Benchmark of a new multi-ion-species collision operator for δf Monte Carlo neoclassical simulation. *Computer Physics Communications*, 255:107249, 2020.
- [30] K. Fujita, S. Satake, R. Kanno, M. Nunami, M. Nakata, and J.M. García-Regaña. Global effects on the variation of ion density and electrostatic potential on the flux surface in helical plasmas. *Plasma and Fusion Research*, 14:3403102, 2019.
- [31] K. Fujita, S. Satake, R. Kanno, M. Nunami, M. Nakata, J. M. García-Regaña, J. L. Velasco, and I. Calvo. Global calculation of neoclassical impurity transport including the variation of electrostatic potential. *Journal of Plasma Physics*, 86(3):905860319, 2020.
- [32] H. Sugama, T-H. Watanabe, and M. Nunami. Linearized model collision operators for multiple ion species plasmas and gyrokinetic entropy balance equations. *Physics of Plasmas*, 16(11):112503, 2009.
- [33] H. Sugama, S. Matsuoka, S. Satake, M. Nunami, and T-H Watanabe. Improved linearized model collision operator for the highly collisional regime. *Physics of Plasmas*, 26(10):102108, 2019.
- [34] D. A. Spong. Generation and damping of neoclassical plasma flows in stellarators. *Physics of Plasmas*, 12(5):056114, 2005.
- [35] J. M. García-Regaña, T. Estrada, I. Calvo, J. L. Velasco, J. A. Alonso, D. Carralero, R. Kleiber, M. Landreman, A. Mollén, E. Sánchez, C. Slaby, TJ-II team, and W7-X team. On-surface potential and radial electric field variations in electron root stellarator plasmas. *Plasma Physics and Controlled Fusion*, 60(10):104002, 2018.
- [36] D. E. Hastings, W. A. Houlberg, and K. C. Shaing. The ambipolar electric field in stellarators. *Nuclear Fusion*, 25(4):445, 1985.
- [37] S. Satake, R. Kanno, and H. Sugama. Development of a non-local neoclassical transport code for

- helical configurations. *Plasma and Fusion Research*, 3:S1062–S1062, 2008.
- [38] M. Yoshinuma, K. Ida, and M. Yokoyama. Impurity transport of ion ITB plasmas on LHD. Technical report, National Inst. for Fusion Science, 2010.
- [39] K. Nagaoka, H. Takahashi, S. Murakami, H. Nakano, Y. Takeiri, H. Tsuchiya, M. Osakabe, K. Ida, M. Yokoyama, M. Yoshinuma, et al. Integrated discharge scenario for high-temperature helical plasma in LHD. *Nuclear Fusion*, 55(11):113020, 2015.
- [40] K. C. Shaing. Test of tokamak low-mode–high-mode transition theory in stellarators. *Physics of Fluids B: Plasma Physics*, 5(11):3841–3843, 1993.
- [41] H. Dahi, J. N. Talmadge, and J. L. Shohet. Effects of plasma parameters on viscosity. *IEEE transactions on plasma science*, 26(6):1738–1744, 1998.
- [42] J. L. Velasco, I. Calvo, F. I. Parra, and J. M. García-Regaña. KNOSOS: A fast orbit-averaging neoclassical code for stellarator geometry. *Journal of Computational Physics*, 418:109512, 2020.
- [43] I. Calvo, F. I. Parra, J. L. Velasco, and J. A. Alonso. The effect of tangential drifts on neoclassical transport in stellarators close to omnigenity. *Plasma Physics and Controlled Fusion*, 59(5):055014, 2017.
- [44] J. Alonso, I. Calvo, J. M. García-Regaña, and J. L. Velasco. Can we use the variations of the electrostatic potential along flux surfaces to control impurity transport in stellarators? 2017. url: <https://www-thphys.physics.ox.ac.uk/research/plasma/JPP/papers17/alonso.pdf>.
- [45] C. D. Beidler and W. D. D’haeseleer. A general solution of the ripple-averaged kinetic equation (gsrake). *Plasma physics and controlled fusion*, 37(4):463, 1995.
- [46] D. E. Hastings. A differential equation for the ambipolar electric field in a multiple-helicity torsatron. *The Physics of fluids*, 28(1):334–337, 1985.
- [47] K. Itoh, H. Sanuki, S. Toda, M. Yokoyama, S.-I. Itoh, M. Yagi, and A. Fukuyama. Transition of radial electric field in helical systems. *Journal of the Physical Society of Japan*, 70(6):1575–1584, 2001.
- [48] S. Toda and K. Itoh. Theoretical study of the hysteresis characteristic of electric fields in helical plasmas. *Plasma physics and controlled fusion*, 46(7):1039, 2004.
- [49] S. Toda. Theory and simulation studies of stationary and dynamical phenomena with transition in helical plasmas. In *AIP Conference Proceedings*, volume 1993, page 020005. AIP Publishing LLC, 2018.
- [50] J. L. Velasco, I. Calvo, F. I. Parra, J. A. Alonso, D. Carralero, T. Estrada, J. M. García-Regaña, X. Huang, S. Morita, S. Satake, et al. Fast calculation of neoclassical transport of energy and impurities in arbitrary stellarator geometry with the code KNOSOS. In *22nd ISHW*, (Madison, United States of America 23-27 September), 2019.
- [51] D. A. Spong, J. H. Harris, A. S. Ware, S. P. Hirshman, and L. A. Berry. Shear flow generation in stellarators—configurational variations. *Nuclear Fusion*, 47(7):626, 2007.
- [52] H. Yamaguchi and S. Murakami. Electrostatic potential generated by perpendicular neutral-beam injection to a tokamak plasma. *Nuclear Fusion*, 58(1):016029, 2017.
- [53] P. Manas, A. Kappatou, C. Angioni, R. M. McDermott, et al. Light impurity transport in tokamaks: on the impact of neutral beam fast ions. *Nuclear Fusion*, 60(5):056005, 2020.
- [54] M. Nunami, M. Nakata, S. Toda, A. Ishizawa, R. Kanno, and H. Sugama. Simulation studies on temperature profile stiffness in ITG turbulent transport of helical plasmas for flux-matching technique. *Physics of Plasmas*, 25(8):082504, 2018.
- [55] M. Nunami. Kinetic simulation study to understand the impurity transport. In *Plasma Simulator Symposium 2020*, (Toki, Japan 17 September), 2020.
- [56] M. Nunami, M. Nakata, S. Toda, and H. Sugama. Turbulence simulations for stellarator plasma transport. In *SPIG 2020*, (Šabac, Serbia, 24-48 August), 2020.